JOURNAL OF AIRCRAFT
Vol. 43, No. 1, January–February 2006

Computational Methods for Simulation of Flow Around Helicopter Engine Inlet

Yihua Cao,* Kungang Yuan,† and Xiaoyong Li‡
Beijing University of Aeronautics and Astronautics, 100083 Beijing, People's Republic of China

Using the finite volume method, the Navier–Stokes equations are solved on a body-fitted structured grid. The low speed and hovering flight of MI-171V5 helicopter are numerically simulated, and the flowfield characteristics around its engine inlet are calculated. Following this, beginning with a prescribed wake model, a semi-empirical correction for the vortex core effect on rotor wake is made, and a free-wake calculation is carried out. The calculated results show that both computational-fluid-dynamics method and free-wake analytical technique can predict the vortex wake flowfield distributions.

Introduction

WITH the rapid development of computational technology, numerical simulation by solving Navier–Stokes (N-S) equations is playing an important role in rotor aerodynamics. Several problems must be resolved for carrying out numerical simulation of N-S equations, for example, 1) the mathematic description of fluid state—governing equations; 2) the numerical expression of governing equation—calculating schemes; 3) the decomposition of solution space—calculating grid; 4) the description of initial state—boundary condition and initial value; and 5) how to solve huge set of equations—solver. It is well known that there are some research papers on rotor flow and interaction between rotor and fuselage. However, for computational-fluid-dynamics (CFD) technology, there are few publications about studying the coupled rotor/fuselage flows, especially the flow around engine inlet. To enhance engine operation safety in helicopter NOE (nap of Earth) flight, it is necessary to reduce the probability of weed entering engine. Therefore, in this paper the flow around helicopter engine inlet is numerically simulated by solving N-S equations for the first time so as to preliminarily understand the flow pattern of weed entering engine for helicopter NOE flight. The numerical simulation results are also preliminarily analyzed and validated.

However, proceeding from the particularity of rotor aerodynamics, vortex modeling for rotor aerodynamics is still a viable approach for delineating problem areas and very useful for guiding further theoretical and experimental investigations.[1] As for the vortex modeling for rotor aerodynamics, it means rotor vortex theory (i.e., in other words, rotor-wake analytical method). At present, there are three kinds of wake analytical methods including prescribed-wake, free-wake, and half-free-wake analytical methods.[2–4] Beginning with the generalized prescribed wake model,[2] the tip vortex core effect on vortex self-induced velocity is introduced,[5–8] and a free wake is calculated. Then, on the condition of circulation and wake geometry convergence, the rotor thrust is calculated to satisfy convergence criterion of thrust. Finally, as an example of engineering, the induced flowfield around the helicopter engine inlet based on wake geometry results is calculated. The calculated result is compared with one of N-S numerical simulation and analyzed.

Received 19 November 2004; revision received 4 February 2005; accepted for publication 14 February 2005.

*Professor, Department of Flight Vehicle Design and Applied Mechanics.
†Doctoral Candidate, Department of Flight Vehicle Design and Applied Mechanics.
‡Masters Candidate, Department of Flight Vehicle Design and Applied Mechanics.

Method Description

Numerical Simulation of N-S Equations

Governing Equations

The compressible N-S equations can be represented in the following forms:

Continuity equation:

$$\frac{\partial \rho}{\partial t} + \nabla \cdot (\rho \boldsymbol{V}) = 0 \tag{1}$$

Momentum equation:

$$\rho \frac{\partial \boldsymbol{V}}{\partial t} + \rho(\boldsymbol{V} \cdot \nabla)\boldsymbol{V} = \rho \boldsymbol{f} - \nabla p + \nabla(\lambda \nabla \cdot \boldsymbol{V}) + \nabla \cdot \mu[\varepsilon] \tag{2}$$

Energy equation:

$$\rho \frac{\partial h}{\partial t} + \rho(\boldsymbol{V} \cdot \nabla)h = \frac{\partial p}{\partial t} + (\boldsymbol{V} \cdot \nabla)p + \Phi + \nabla \cdot (k \nabla T) \tag{3}$$

where

$$[\varepsilon] = \begin{bmatrix} 2\dfrac{\partial u}{\partial x} & \left(\dfrac{\partial u}{\partial y} + \dfrac{\partial v}{\partial x}\right) & \left(\dfrac{\partial u}{\partial z} + \dfrac{\partial w}{\partial x}\right) \\ \left(\dfrac{\partial v}{\partial x} + \dfrac{\partial u}{\partial y}\right) & 2\dfrac{\partial v}{\partial y} & \left(\dfrac{\partial v}{\partial z} + \dfrac{\partial w}{\partial y}\right) \\ \left(\dfrac{\partial w}{\partial x} + \dfrac{\partial u}{\partial z}\right) & \left(\dfrac{\partial w}{\partial y} + \dfrac{\partial v}{\partial z}\right) & 2\dfrac{\partial w}{\partial z} \end{bmatrix} \tag{4}$$

$$\Phi = \lambda\left(\frac{\partial u}{\partial x} + \frac{\partial v}{\partial y} + \frac{\partial w}{\partial z}\right)^2 + \mu\left[2\left(\frac{\partial u}{\partial x}\right)^2 + 2\left(\frac{\partial v}{\partial y}\right)^2 + 2\left(\frac{\partial w}{\partial z}\right)^2 + \left(\frac{\partial v}{\partial x} + \frac{\partial u}{\partial y}\right)^2 + \left(\frac{\partial w}{\partial y} + \frac{\partial v}{\partial z}\right)^2 + \left(\frac{\partial u}{\partial z} + \frac{\partial w}{\partial x}\right)^2\right] \tag{5}$$

There are six variables in preceding equations (p, ρ, T, u, v, w), whereas only five equations exist. For the solution of these equations, the perfect-gas state equation should be employed as follows:

$$p = \rho R T \tag{6}$$

Commonly, the volume force $\boldsymbol{f}$ involves gravity, and it is often ignored, where μ represents the viscous coefficient and k is the heat-conductive coefficient.

Calculating Scheme

Using the finite volume method, the N-S equations in integral form can be described as follows:

$$\frac{\partial}{\partial t}\int_{\Omega} U d\Omega + \int_{\Gamma} \boldsymbol{W} \cdot \boldsymbol{n} d\Gamma = 0 \tag{7}$$

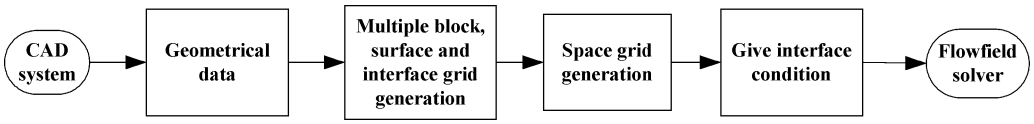

Fig. 1 Process of grid generation.

where

$$U = [\rho, \rho u, \rho v, \rho w, E]^T \tag{8}$$

$$\boldsymbol{W} = \begin{Bmatrix} \rho \boldsymbol{V} \\ \rho u \boldsymbol{V} + (p - \tau_{xx})\boldsymbol{i} - \tau_{yx}\boldsymbol{j} - \tau_{zx}\boldsymbol{k} \\ \rho v \boldsymbol{V} - \tau_{xy}\boldsymbol{i} + (p - \tau_{yy})\boldsymbol{j} - \tau_{zy}\boldsymbol{k} \\ \rho w \boldsymbol{V} - \tau_{xz}\boldsymbol{i} - \tau_{yz}\boldsymbol{j} + (p - \tau_{zz})\boldsymbol{k} \\ (E + p)\boldsymbol{V} - (\tau_{xx}u + \tau_{xy}v + \tau_{xz}w)\boldsymbol{i} \\ -(\tau_{yx}u + \tau_{yy}v + \tau_{yz}w)\boldsymbol{j} \\ -(\tau_{zx}u + \tau_{zy}v + \tau_{zz}w)\boldsymbol{k} - k\nabla T \end{Bmatrix} \tag{9}$$

where $\boldsymbol{V} = u\boldsymbol{i} + v\boldsymbol{j} + w\boldsymbol{k}$ represents velocity vector: $E = \rho(e + |\boldsymbol{V}|^2/2)$; e is inner energy per unit mass; Ω is flow area; and Γ is boundary of flow area.

For each volume, Eq. (7) comes into existence after dividing the flowfield into finite volumes, and so the variables U can be solved through establishing difference equations.

Grid Generation

The grid-generation technique is an important branch in computational-fluid-dynamics development. There are several kinds of grids, such as Cartesian orthogonal grid, structured (body-fitted) grid, and unstructured grid. The structured (body-fitted) grid is used in this investigation.

It is difficulty to generate single-zone structured (body-fitted) grids as the configuration becomes more and more complex. Therefore, multiblock structured grid and unstructured grid appeared recently and have been widely used in complex flow computations.

The process of multiple block grid generation is shown as Fig. 1.

In this paper the grid generation is completed over a domain size of (4 × 4 × 2) rotor diameters, and the computational domain centered around rotor hub center in three (length × width × height) directions. As for the ground effect in NOE flight, the bottom surface of the computational domain is chosen as the ground.

Boundary Condition and Initial Value

There are two kinds of boundaries: physical boundary and artificial boundary. Physical boundary is imposed by nature because it is confirmed by physical properties. Artificial boundary is set for the infinite or semi-infinite area, or when the interested area is far less than the practical area. There are mainly four methods to deal with infinite flow boundary: zone transformation method, finite truncation method, small disturbance method, and analytical boundary method.[9,10] In this paper, finite truncation method is used to deal with infinite flow boundary (i.e., outlet boundary of back surface). An analytical boundary method is used to deal with the upper surface boundary of the computational domain (i.e., rotor vertical inflow inlet condition), for example, implementation of inflow velocity condition is determined by means of rotor vortex theory.

Initial value presents fluid parameter value at $t = 0$. In this paper, as for CFD methodology, it is first based on the SIMPLE algorithm of FLUENT-CFD software, and then actuator disc modeling for helicopter rotor and previous methods[11–14] are synthetically used. At the same time, the downwash velocity is acquired from free-vortex-wake technique.[8]

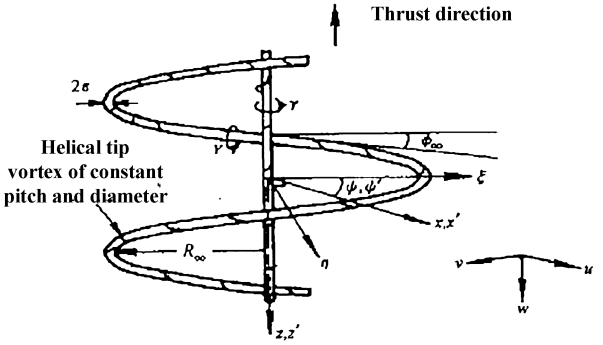

Fig. 2 Schematic of vortex core element.

Vortex Modeling Method for Rotor Aerodynamics

Generalized Wake Model

The tip vortex location can be simulated by a series of linear and exponential functions. For a hovering rotor, prescribed and generalized wake can be expressed as follows[2]:

The tip vortex axial coordinate is

$$Z = \begin{cases} k_1 \Psi_w & 0 \le \Psi_w \le 2\pi/N_b \\ k_1 2\pi/N_b + k_2(\Psi_w - 2\pi/N_b) & \Psi_w \ge 2\pi/N_b \end{cases} \tag{10}$$

The tip vortex radial coordinate is

$$r = A + (1 - A)e^{-\lambda \Psi_w} \tag{11}$$

Inner vortex sheet axial coordinate is

$$Z = Z_{r=0} + r(Z_{r=1} - Z_{r=0}) \tag{12}$$

where

$$Z_{r=1} = \begin{cases} k_{11}\psi_w & 0 \le \psi_w \le 2\pi/N_b \\ k_{11}(2\pi/N_b) + k_{21}(\psi_w - 2\pi/N_b) & \psi_w \ge 2\pi/N_b \end{cases}$$

$$Z_{r=0} = \begin{cases} 0 & 0 \le \psi_w \le \pi/2 \\ k_{20}(\psi_w - 2\pi/N_b) & \psi_w > \pi/2 \end{cases}$$

Inner vortex sheet radial coordinate is

$$r = r_C \cdot r_B / r_D \tag{13}$$

Vortex Core Effects

Using free-wake analytical idea, tip vortex evolves freely in air environment. Tip vortex element's induced velocity is contributed by blade bound vortex, inner vortex sheet, and tip vortex itself. Based on the Biot–Savart law, the nondimensional induced velocity caused by a vortex element at any calculated point can be described in cylindrical polar coordinate as follows (see Fig. 2):

The radial-induced velocity component is

$$\bar{u} = \frac{C_{\Gamma F}}{C_\Gamma} \times \int \begin{Bmatrix} x'^2 \tan\phi' \sin(\psi' - \psi) + [x' \tan\beta' \sin(\psi' - \psi) \\ + x' \cos(\psi' - \psi)][Z - Z'] \end{Bmatrix} \frac{d\psi'}{p^3} \tag{14}$$

The circumferential-induced velocity component is

$$\bar{v} = \frac{C_{\Gamma F}}{C_\Gamma} \times \int \left\{ \begin{array}{l} x'^2 \tan\phi'[x - x'\cos(\psi' - \psi)] - [x' \tan\beta' \cos(\psi' - \psi) \\ \quad - x' \sin(\psi' - \psi)][Z - Z'] \end{array} \right\} \times \frac{\mathrm{d}\psi'}{p^3} \tag{15}$$

The axial-induced velocity component is

$$\bar{w} = \frac{C_{\Gamma F}}{C_\Gamma} \times \int \{x'^2 - xx'\cos(\psi' - \psi) - xx' \tan\beta' \sin(\psi' - \psi)\} \frac{\mathrm{d}\psi'}{p^3} \tag{16}$$

where $p^2 = x'^2 + x^2 - 2xx'\cos(\psi' - \psi) + (z - z')^2 + \varepsilon^2$.

The variables with prime symbol ‘ represent the coordinates at any point of vortex element centric line and respective pitch angle. The variables without prime symbol ‘ represent the coordinates at the calculated points. ε is the vortex core diameter of vortex element. It is apparent that for tip vortex element p value does not equal to zero because the vortex core diameter is introduced, and so the calculated point is kept outside the tip vortex surface and integration for induced velocity is a precise value.

Based on general knowledge about rotor vortex systems, inner vortex sheet thickness is varying in space and with time. Tip vortex can be qualitatively regarded as a space helix that is formed of the wound vortex lines near blade tip. The cross-section shape of tip vortex core is very complex, and the tip vortex centric line is a contracting helical line in space. At the same time, vorticity distribution inside the tip vortex core is not symmetrical or uniform with respect to centric line. It is apparent that it is very complicated and difficult to describe such vortex system by means of mathematics. In this paper, inner sheet is modeled as zero-thickness vortex sheet, and tip vortex is described as a simplified model. In this way, tip vortex is represented by a space helix with constant vortex core diameter, and its vorticity is concentrated at the centric line with a constant value (see Fig. 2).

For such a space helical vortex element, the axial-induced velocity caused by vortex core effect at its middle point is[5–7]

$$\bar{w}_c = \frac{2\cos\delta}{p_L} \left\{ \ell_n \frac{4p_L}{\varepsilon} - \frac{1}{4} - \frac{k^2 \sin(\theta/2)\cos(\theta/2)}{[1 - k^2\cos^2(\theta/2)]^{\frac{1}{2}}} - \ell_n \left[\frac{1 + \cos(\theta/2)}{\sin(\theta/2)} \right] + \cos\frac{\theta}{2} \right\} \tag{17}$$

where δ is the angle of inclination of vortex element with respect to rotor axial direction: $\tan\delta = \psi_0 \tan\varphi_\infty / \sin\psi_0$. ψ_0 is the circumferential angle between the calculated point and the first neighboring radial plane:

$$\sin\theta = (1 - \tan^2\delta)\sin\psi_0 \cos\delta \Big/ \left(1 + \cos^2(\psi_0/2)\tan^2\delta\right)$$
$$p_L^2 = 4\left[1 + \cos^2(\psi_0/2)\tan^2\delta\right]^2 + \varepsilon^2$$
$$k^2 = 1 - \varepsilon^2 \Big/ p_L^2$$

The contribution of vortex core effect to the circumferential induced velocity is

$$\bar{v}_c = -\bar{w}_c \tan\delta \tag{18}$$

According to formula (11), the contribution of vortex core effect to the radial induced velocity can be approximately expressed by following formula:

$$\bar{u}_c = \bar{u}(C/A)e^{-\lambda\psi_w} \tag{19}$$

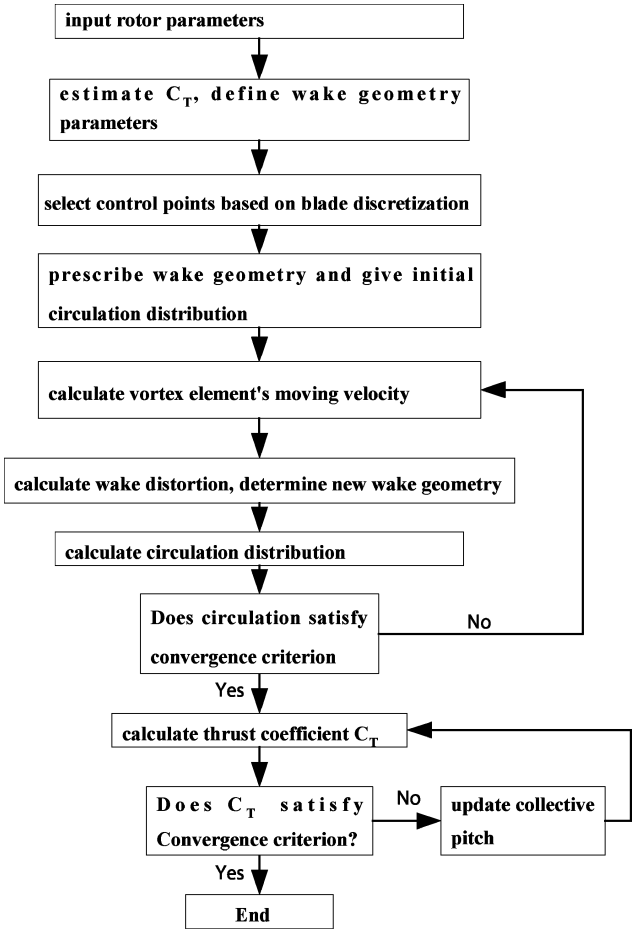

Fig. 3 Free-wake analysis block diagram.

Free-Wake Analytical Technique

In cylindrical polar coordinates, new geometry coordinates can be defined as[8]

$$\left. \begin{array}{r} \psi_{(i+1)}^{new} = \psi_{(i)}^{old} + v(i)\Delta t / r(i) \\ r_{(i+1)}^{new} = r_{(i)}^{old} + u(i)\Delta t \\ z_{(i+1)}^{new} = z_{(i)}^{old} + w(i)\Delta t \end{array} \right\} \tag{20}$$

The free-wake analysis block diagram is shown in Fig. 3.

Wake-geometry convergence criterion is replaced by circulation convergence criterion in this paper. The circulation convergence criterion can be described as

$$\text{error} = \frac{\sum_{i=1}^{Ne} \left[\Gamma_{(i)}^{new} - \Gamma_{(i)}^{old}\right]^2}{\sum_{i=1}^{Ne} \left[\Gamma_{(i)}^{new}\right]^2} \le \delta_0 \tag{21}$$

where δ_0 can be generally taken as $\delta_0 = 5.0 \times 10^{-5}$, its selection depends on the compromise between the calculating time and accuracy requirement.

In forward flight the helical vortices trailed from the blade are carried rearward by the freestream velocity component parallel to the disk (μ) as well as downward by the component normal to the disk (λ) (see Fig. 4). The wake skew angle $\chi = \tan^{-1}(-\lambda/\mu)$ can be estimated well using moment theory, and so the initial rotor wake geometry in forward flight for iterative calculation can be first constructed by tilting rearward hovering rotor-wake geometry (the cylindrical wake geometry) according to wake skew angle, and then real wake geometry can be obtained by free-wake calculation technique. As for downwash velocity field, based on Biot–Savart law, the downwash velocity induced by bound vortex and trailing vortices for any point can be calculated.

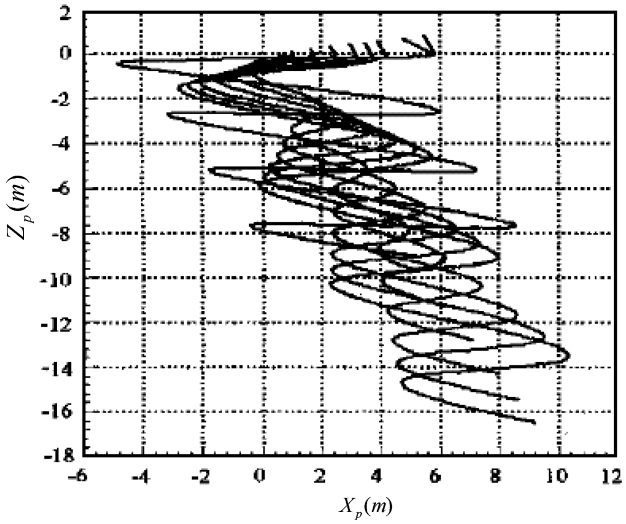

Fig. 4 Rotor-wake geometry in forward flight ($\mu = 0.02$).

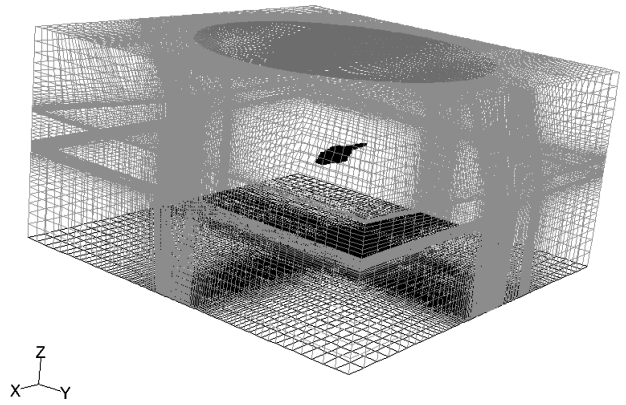

Fig. 5a Whole grid for helicopter flow simulation.

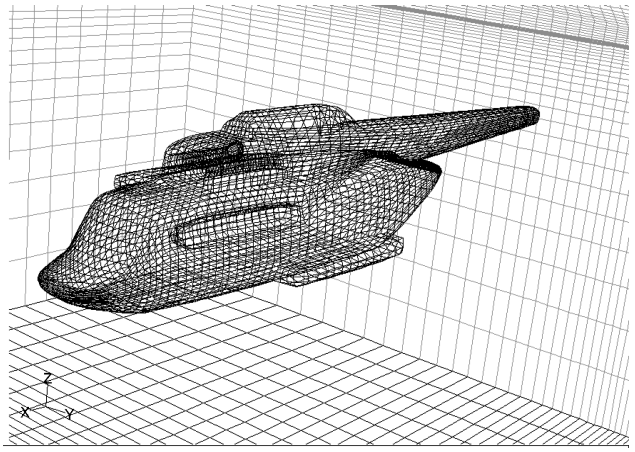

Fig. 5b Helicopter surface grid.

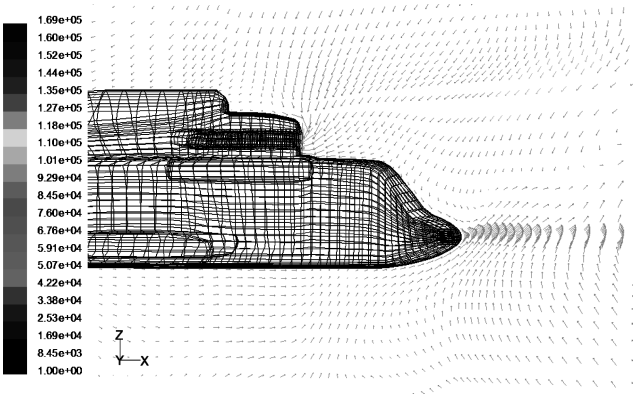

Fig. 6a Longitudinal flow pattern around helicopter left engine at hover.

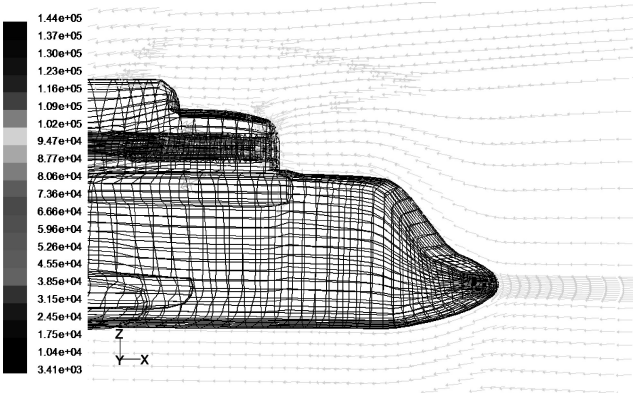

Fig. 6b Longitudinal flow pattern around helicopter left engine in forward flight ($\mu = 0.05$).

Calculated Results

N-S Equations Numerical Simulation Results

Grid Generation and Numerical Calculation

To correlate with data of a sample MI-171V5 helicopter with five-bladed rotor (rotor diameter $D = 21.3$ m, rotor rotational speed $\Omega = 20.096$ rad/s), the model geometry is established, and the calculating grid is generated. The grid-generation process is a gradual approach process that needs testing and amending many times.

The total numbers of calculating grids are 1.205 million (see Figs. 5a and 5b).

The other parameters for N-S equations simulation are set as follows:

1) Using the ideal-gas model, the gas parameters must be consistent with ones from gas dynamics handbooks.

2) No-slip boundary condition is used on helicopter surface.

Calculation Results and Analyses

The flowfield characteristics of MI-171V5 helicopter at hover and in forward flight can be found according to velocity vector plots (see Figs. 6–8). Because of the effects of rotor downwash and engine, the flow velocity of the air entering into engine is increased as compared with one of the air at freestream, while its pressure decreases. Furthermore, velocity profile of the air entering into engine in forward flight is different from one at hover (see Figs. 6a and 6b), and the former is stronger. It can be apparently seen that vortex flow exists at hover in the lateral flow patterns of helicopter (see Figs. 7 and 8), and the flow entering into engine inlet is clearly obtained both at hover and in forward flight. In effect, because of the existence of an additional kerosene stove on right side of helicopter body, flow structures on two sides of helicopter are not symmetrical, and air velocity entering into right engine is increased. At the same time, vortex ingestion is apparently seen on the upper of left engine (seeing Figs. 7a and 8a). These calculation results are well consistent with fluid-dynamics theory.

Results from Vortex Modeling Method for Rotor Aerodynamics

Rotor Downwash Flowfield Grids

According to the engine location relative to MI-171V5 helicopter rotor, grids for rotor downwash flowfield can be constructed in engine body coordinates $S_t(O_t X_t Y_t Z_t)$ (see Fig. 9):

1) X_t direction: $-11.00 \le X_t \le 1.00$, $\Delta X_t = 0.5$.

2) Y_t direction: $0.00 \le Y_t \le 0.30$, $\Delta Y_t = 0.3$; $0.30 \le Y_t \le 0.50$, $\Delta Y_t = 0.2$; and $0.50 \le Y_t \le 7.00$, $\Delta Y_t = 0.5$.

3) Z_t direction: $-3.000 \le Z_t \le 1.10$, $\Delta Z_t = 0.5$.

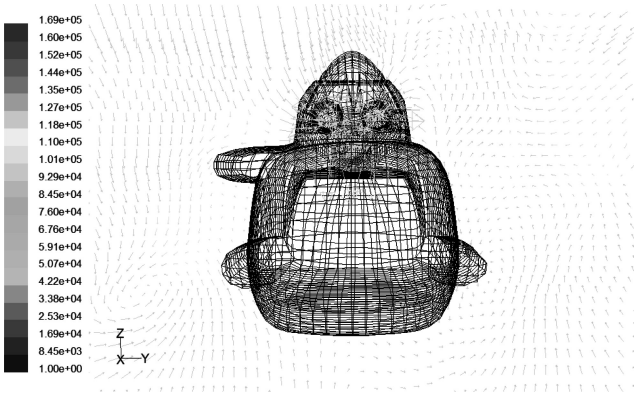

Fig. 7a Lateral flow pattern around helicopter engine inlet at hover.

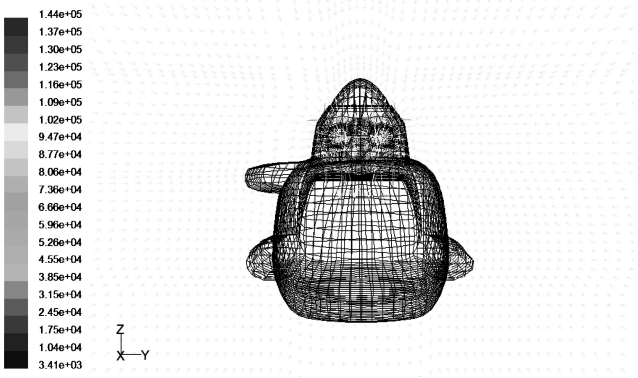

Fig. 7b Lateral flow pattern around helicopter engine inlet in forward flight ($\mu = 0.05$).

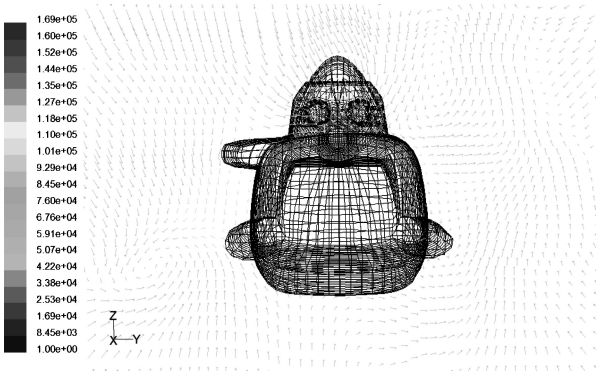

Fig. 8a Lateral flow pattern around the cross section at 0.4 m forward from engine inlet at hover.

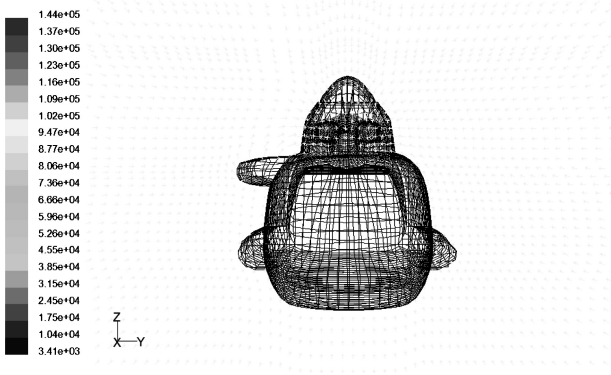

Fig. 8b Lateral flow pattern around the cross section at 0.4 m forward from engine inlet in forward flight ($\mu = 0.05$).

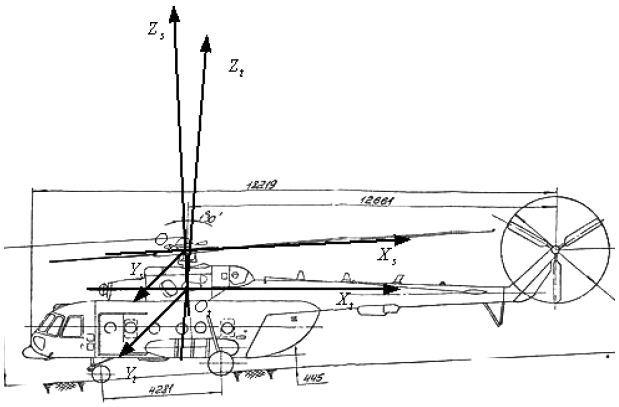

a)

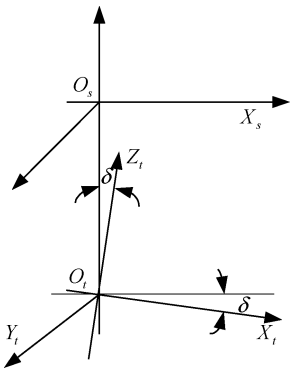

b)

Fig. 9 Coordinates for rotor downwash flowfield calculation.

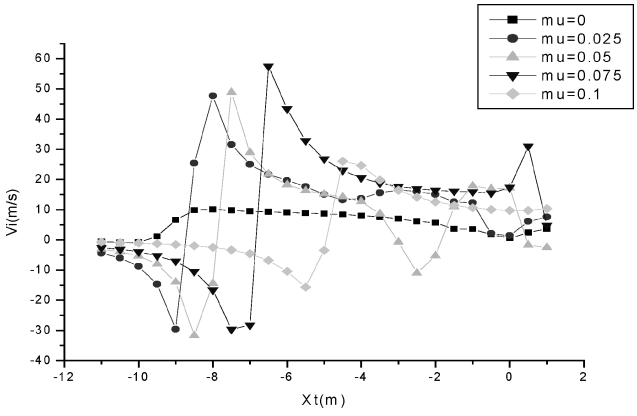

Fig. 10 Rotor downwash velocity distributions at engine centerline.

Then there are $25 \times 16 \times 13 = 5200$ grid points in the calculated area.

Calculated Results for Rotor Downwash Flowfield

It can be seen in Fig. 10 that along the engine centerline, from rotor forward slipstream boundary (for example, boundary point $X_t \approx -9$ m at $\mu = 0.025$) to forward far field, the velocity gradually changes from upwash to zero in forward flight, whereas at hover changes from downwash velocity to zero. The variation trend of these results is similar to that of the measured airflow velocities along rocket trajectory.[15]

Furthermore, from rotor forward slipstream boundary to rearward far field, rotor downwash velocity increases first and then decreases. Figure 11 shows velocity vector plots of rotor downwash flow in helicopter longitudinal plane. The flow pattern of the air entering into engine is preliminarily seen.

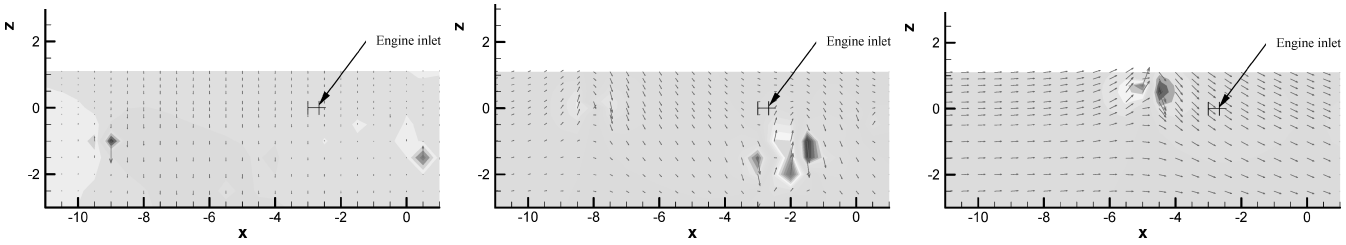

a) $\mu = 0$ **b)** $\mu = 0.05$ **c)** $\mu = 0.1$

Fig. 11 Rotor downwash velocity distributions in engine centric section plane.

Conclusions

In this paper, two methods [i.e., computational-fluid-dynamics (CFD) method and free-wake analytical technique] are used to simulate the rotor flowfield at hover and in forward flight, and the flow characteristics around helicopter engine inlet are presented. The flow directions and velocity vectors around helicopter engine inlet can be distinctly seen from the calculated results. The numerical simulation results can provide the solid basics for experiment planning and engineering application. At the same time, the obtained flow patterns around helicopter engine inlet here can help helicopter engineers with understanding the flow of weed entering engine for helicopter nap of Earth flight. In short, both CFD method and free-wake analytical technique here can predict the vortex wake flowfield distributions around helicopter engine inlet.

References

[1]Gray, R. B., "Vortex Modeling for Rotor Aerodynamics," *Journal of the American Helicopter Society*, Vol. 37, No. 1, 1992, pp. 8–10.

[2]Landgrebe, A. J., "The Wake Geometry of a Hovering Helicopter Rotor and Its Influence on Rotor Performance," *Journal of the American Helicopter Society*, Vol. 17, No. 4, 1972, pp. 3–15.

[3]Felker, F. F., Quackenbush, T. R., Bliss, D. B., and Light, J., "Comparisons of Predicted and Measured Rotor Performance in Hover Using a New Free Wake Analysis," *Vertica*, Vol. 14, No. 3, 1990, pp. 361–383.

[4]Favier, D., Mba, M. N., Barbi, C., and Maresca, C., "A Free Wake Analysis for Hovering Rotors and Advancing Propellers," *Vertica*, Vol. 11, No. 3, 1987, pp. 493–511.

[5]Samant, S. S., and Gray, R. B., "A Semi-Empirical Correction for the Vortex Core Effect on Hovering Rotor Wake Geometries," American Helicopter Society, Paper No. 77.33-02, May 1977.

[6]Gray, R. B., and Brown, G. W., "A Vortex Wake Analysis of a Single-Bladed Hovering Rotor and a Comparison with Experimental Data," *Proceedings of the AGARD Conference on Aerodynamics of Rotary Wings, Fluid Dynamics Panel Specialists Meeting*, AGARD-Cp-111, Paper No. 4, Sept. 1972.

[7]Lamb, H., *Hydrodynamics*, Dover, New York, 1945, pp. 210–241.

[8]Cao, Y., "A New Method for Predicting Rotor Wake Geometries and Downwash Velocity Field," *Aircraft Engineering and Aerospace Technology: an International Journal*, Vol. 71, No. 2, 1999, pp. 129–135.

[9]Versteeg, H. K., and Malalasekera, W., *An Introduction to Computational Fluid Dynamics—The Finite Volume Method*, Longman Group, Ltd., England, U.K., 1995, pp. 192–209.

[10]Anderson, J. D., Jr., *Computational Fluid Dynamics—The Basics with Applications*, McGraw–Hill Co., Inc., Columbus, 1995, pp. 13–82.

[11]Le Chuiton, F., "Actuator Disc Modeling for Helicopter Rotors," *Aerospace Science and Technology*, Vol. 8, No. 4, 2004, pp. 285–297.

[12]Cao, Y., and Su, Y., "Insight into the Effects of Rotor Downwash on Engine Jet," *Aircraft Engineering and Aerospace Technology: An International Journal,* Vol. 75, No. 4, 2003, pp. 345–349.

[13]Cao, Y., Wang, J., and Su, Y., "Mixed Jameson/Total-Variation-Diminishing Scheme Applied to Simulating Rotor Airfoil Flowfield," *Journal of Aircraft*, Vol. 40, No. 1, 2003, pp. 213–216.

[14]Cao, Y., Yu, Z., and Su, Y., "A Coupled Free Wake-CFD Method for the Simulation of Helicopter Rotor Flow," *Canadian Aeronautics and Space Journal*, Vol. 48, No. 4, 2002, pp. 251–258.

[15]Landgrebe, A. J., Taylor, R. B., and Egolf, T. A., "Helicopter Airflow and Wake Characteristics for Low Speed and Hovering Flight," *Journal of the American Helicopter Society*, Vol. 27, No. 4, 1982, pp. 74–83.